nature communications

Article

https://doi.org/10.1038/s41467-025-64064-z

Amplified copper ion interference and immunomodulation using self-thermophoretic nanomotors to treat refractory implant-associated biofilm infections

Received: 22 December 2024

Accepted: 5 September 2025

Liuliang He[1,6], Qiyong Pan[1,6], Mingfei Li[1], Zhichao Wang[1], Long Wang[1], Chi Zhang[1] ✉, Zhi-Hao Wang[2,3,4,5] ✉, Jinjin Shi[2,3,4,5] ✉ & Daifeng Li[1] ✉

Orthopedic implant-associated biofilm infections (IABIs) are refractory to elimination because of the dense biofilm formation and local immunosuppressive microenvironment. Herein, we propose a copper-based therapeutic strategy to treat IABIs. Initially, the *Janus* bisphere nanostructure is fabricated using mesoporous silicon nanoparticle (MSN) with gold nanoparticle. Subsequently, copper peroxide (CP) nanodots are encapsulated within the MSN to form the final nanomotor Motor@CP. Our Motor@CP exhibits remarkable autonomous movement through near-infrared (NIR)-propelled self-thermophoretic propulsion, effectively penetrating dense biofilms and delivering CP. Notably, the acidic microenvironment facilitates CP decomposition into copper(II) and hydrogen peroxide. This process further generates hydroxyl radicals (•OH), extensively destroying biofilm integrity and enhancing intracellular uptake of copper ions that trigger bacterial cuproptosis-like death. Furthermore, Motor@CP markedly reprograms infiltrating macrophages toward pro-inflammatory phenotypes, thereby promoting an antimicrobial immune response. Overall, this presents a promising approach that leverages amplified copper ion interference and macrophage reprogramming to combat refractory orthopedic IABIs.

Orthopedic implant-associated biofilm infections (IABIs) are the leading cause of surgical failure in orthopedic procedures and pose a significant, ongoing challenge in clinical practice[1–3]. Unfortunately, IABIs are refractory to elimination and show a high risk of relapse rate because of dense microbial biofilms formed on the implant, which call for large amounts of antibiotics and multiple revision surgeries, bringing tremendous physical and mental torture to patients[4,5]. Moreover, common pathogens such as *Staphylococcus aureus* (*S. aureus*) and methicillin-resistant *S. aureus* (MRSA), which reside within biofilm shelters, exhibit robust resistance to conventional antibiotics

---

[1]Department of Orthopedics, The First Affiliated Hospital of Zhengzhou University, Zhengzhou, China. [2]School of Pharmaceutical Sciences, Zhengzhou University, Zhengzhou, China. [3]Key Laboratory of Advanced Drug Preparation Technologies, Ministry of Education, Zhengzhou, China. [4]State Key Laboratory of Antiviral Drugs, Pingyuan Laboratory, Zhengzhou University, Zhengzhou, China. [5]Henan Key Laboratory of Targeting Therapy and Diagnosis for Critical Diseases, Zhengzhou, China. [6]These authors contributed equally: Liuliang He, Qiyong Pan. ✉e-mail: zhangchi211@zzu.edu.cn; wangzhihao@zzu.edu.cn; shijinyxy@zzu.edu.cn; lidaifeng@zzu.edu.cn

and innate host immunity responses[6,7]. Additionally, the highly acidic, hypoxic, and nutrient-depleted biofilm microenvironment (BME) compromises local immunological competence and promotes the polarization of pro-inflammatory immune cells toward anti-inflammatory phenotypes, further complicating antibiofilm therapeutic strategies[8–10]. Therefore, developing antibiotic-free treatments that can effectively disrupt biofilms while reprogramming immune cells holds great promise for achieving improved therapeutic outcomes for IABIs with minimal risk of drug resistance.

Recently, a variety of nanomaterials that simultaneously exhibit antimicrobial properties and immunomodulatory effects have been investigated[11,12]. Copper serves as an essential cofactor for all living organisms, playing a critical role in numerous biochemical processes. However, when its concentration exceeds the threshold regulated by evolutionarily conserved homeostatic mechanisms, copper becomes toxic and disrupts bacterial metabolism[13,14]. Specifically, the accumulation of copper within cellular structures interacts with lipid-acylated components of the tricarboxylic acid cycle (TCA), initiating cuproptosis in cells and cuproptosis-like death in bacteria, thereby providing insights into copper-based therapeutic nanomaterials[15–18]. Moreover, copper ions can generate reactive oxygen species (ROS) via a Fenton-like reaction upon exposure to BME. This process enhances macrophage immune function by facilitating chemotaxis toward planktonic bacteria escaping from disintegrating biofilms through phagocytosis and the release of pro-inflammatory cytokines[19]. Consequently, due to their direct antimicrobial capabilities coupled with their excellent reprogramming effect on immune cells, copper ion-based treatments are considered promising candidates for antibiotic-free treatment options in the post-antibiotic era[20]. Copper peroxide (CP) nanodots represent emerging candidates as copper ion donors. Under acidic conditions, these CP nanodots decompose into copper(II) along with hydrogen peroxide (H_2O_2), which subsequently generates hydroxyl radicals (•OH)[21,22]. These radicals contribute to disrupting bacterial membrane integrity, thereby enhancing copper uptake while promoting cuproptosis[18,19].

However, the efficacy of copper ions is significantly influenced by intracellular copper accumulation within bacteria, primarily due to two key factors: (1) The dense biofilms formed on implants limit the penetration efficiency required for delivering adequate quantities of copper ions[23,24]. (2) Bacteria have developed multiple defense mechanisms, including enhanced efflux systems that expel excess copper and the production of substances that bind available free copper, thereby reducing the internal concentrations capable of inducing cuproptosis-like death[25,26]. Consequently, ensuring effective delivery methods that promote widespread distribution throughout existing mature biofilm remains a critical challenge in IABIs management. Current research primarily focuses on utilizing ROS-generating or hyperthermia-inducing nanocarriers to enhance biofilm permeability and promote the passive bioavailability of relevant ions. However, these innovations still exhibit inadequate biofilm infiltration, particularly in terms of the autonomous diffusion of copper ions within the biofilm. Recently, nanomotors with autonomous movement capabilities have garnered increasing attention due to their exceptional ability to penetrate barriers and deliver drugs effectively[27–30]. Notably, near-infrared (NIR) laser-propelled nanomotors show great potential for overcoming complex physiological barriers, owing to their fuel-free nature and stable motion characteristics, making them promising for a wide range of applications[31,32]. Ji et al. demonstrated that NIR laser-propelled nanomotors exhibited a 3.8-fold higher dermal penetration efficiency compared to passive nanomaterials[33]. Our group also verified that NIR laser-propelled nanomotors achieved a 14.6-fold enhancement in autonomous mucus penetration[29]. Encouraged by these remarkable autonomous movement properties, self-thermophoretic nanomotors propelled by NIR laser irradiation represent a promising strategy for efficiently traversing the biofilm matrix barrier and promoting intracellular copper overload to combat IABIs.

Herein, we introduce a BME-responsive self-thermophoretic *Janus* bisphere nanomotor (Motor@CP) to enhance the eradication of orthopedic IABIs (Fig. 1). Initially, mesoporous silicon nanoparticle (MSN) is utilized as a substrate, while gold nanoparticle (AuNP) serves as a photothermal structure to construct the *Janus* bisphere nanostructure (Motor). Subsequently, CP nanodots are encapsulated within the MSN to form Motor@CP (Fig. 1a). The NIR-propelled Motor@CP exhibits significant autonomous movement through self-thermophoretic propulsion, effectively penetrating dense biofilms in different bacterial species and extensively delivering CP within biofilms. Notably, the Motor@CP explosively decomposes into copper(II) and H_2O_2 in an acidic BME (pH ~ 5.5), subsequently generating •OH via a Fenton-like reaction. Due to its autonomous motion and self-supplying H_2O_2 generation, Motor@CP + NIR substantially disrupts the extracellular DNA (eDNA) component within biofilms, thereby significantly altering their integrity and permeability and facilitating enhanced penetration by Motor@CP. In vitro experiments demonstrate that Motor@CP + NIR increases the intracellular uptake of copper ions in *S. aureus* and *Escherichia coli* (*E. coli*) by 3.4- and 4.1-fold, respectively, while disrupting TCA cycle and inducing extensive cuproptosis-like bacterial death. Additionally, Motor@CP markedly influences infiltrating macrophages, promoting their repolarization toward the pro-inflammatory M1 phenotype and enhancing the antimicrobial immune response (Fig 1b). Collectively, this approach presents a promising antibiotic-free alternative involving amplified copper ion interference and macrophage reprogramming to eradicate refractory orthopedic IABIs.

Results

In vitro antibiofilm efficacy of copper ions and characterization of CP and Motor@CP

Copper, a historically established antimicrobial metal exhibiting dose-dependent antibacterial properties and cytotoxicity, has been extensively utilized for controlling various pathogenic microorganisms[34–36]. Studies have shown that the optimal concentration range of copper ions for antibacterial activity is $0.63\,\mu g\,ml^{-1}$ to $6.3\,\mu g\,ml^{-1}$, which can achieve an antibacterial effect of over 90% and maintain a cell proliferation rate of over 80%[37]. However, it remains unclear whether this concentration range can effectively maintain bactericidal activity against dense bacterial biofilms. We systematically evaluated the antibacterial efficacy of the conventional copper ion donor, cupric chloride dihydrate ($CuCl_2{\cdot}2H_2O$), against both planktonic forms and biofilms of *S. aureus* and MRSA. The concentrations of $CuCl_2{\cdot}2H_2O$ used in the experiment were 2, 4, and $8\,\mu g\,ml^{-1}$, corresponding to copper ion concentrations of 0.746, 1.491, and $2.982\,\mu g\,ml^{-1}$, respectively. These values were within the concentration range reported in previous studies. The antibacterial and antibiofilm efficacy of $CuCl_2{\cdot}2H_2O$ in vitro was evaluated using OD_{600} measurements (Fig. 2a), colony counts on spread plates (Fig. 2b and Supplementary Fig. 1), crystal violet staining (Fig. 2c and Supplementary Fig. 2) and inductively coupled plasma optical emission spectrometry (ICP-OES) (Fig. 2d). At a $CuCl_2{\cdot}2H_2O$ concentration of $2\,\mu g\,ml^{-1}$, 90% of bacterial populations were effectively eradicated (Fig. 2b), which is consistent with previously reported minimum inhibitory concentration (MIC) of copper ions for *S. aureus* ($0.63\,\mu g\,ml^{-1}$)[18]. However, no significant increase in either copper content within biofilms or biofilm eradication was observed following $CuCl_2{\cdot}2H_2O$ treatment in the aforementioned investigations. These findings indicate that while copper ions within the safe concentration range demonstrate effective dose-dependent antibacterial activity against planktonic bacteria; however, they show limited efficacy against biofilms, likely due to the dense extracellular polymeric substance (EPS) of biofilms[38].

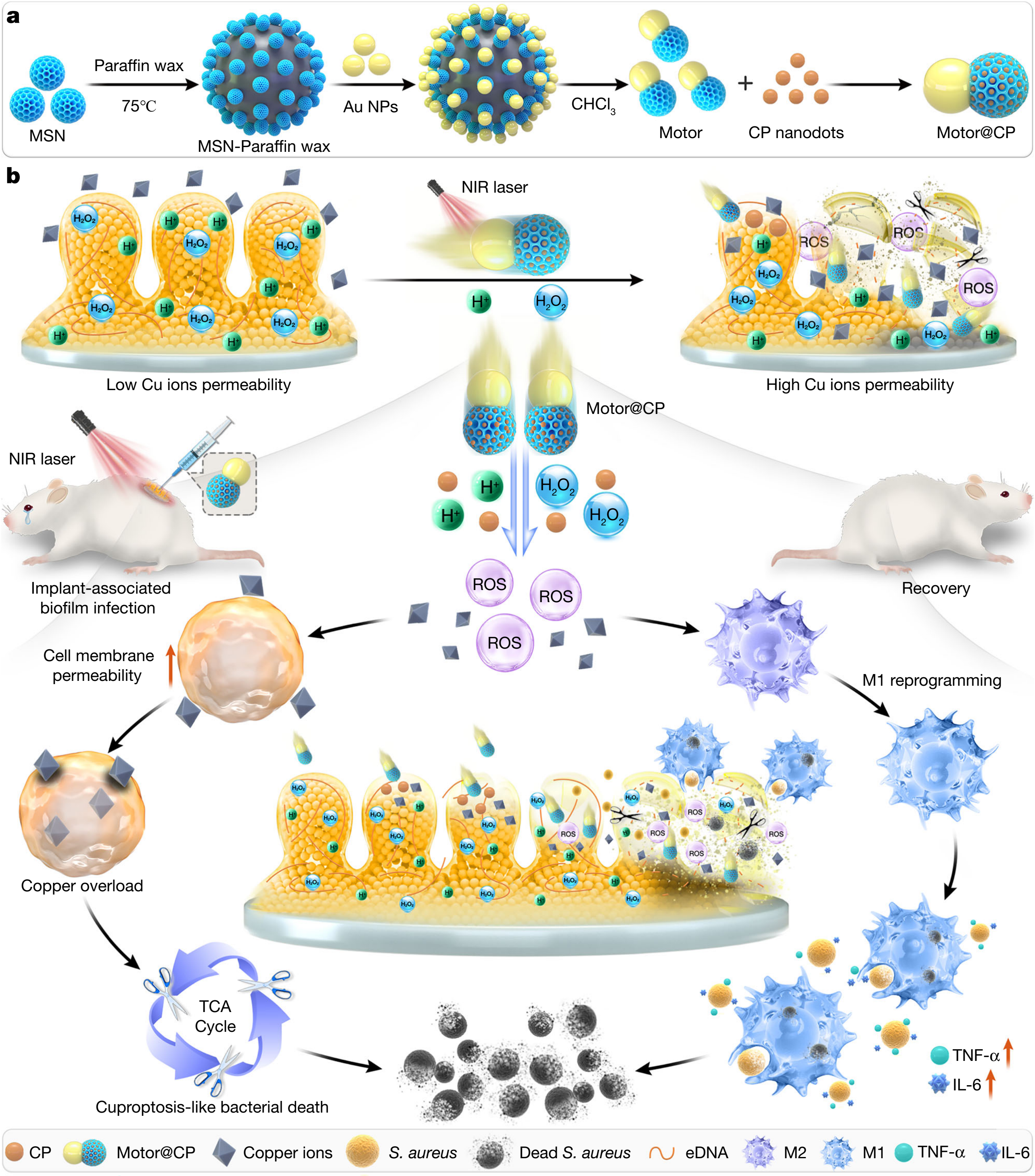

Fig. 1 | Design strategy for BME-responsive self-thermophoretic nanomotor to treat refractory IABIs. a Construction of the Janus bisphere nanostructure Motor@CP. **b** The NIR-propelled Motor@CP exhibits remarkable biofilm penetration and significant autonomous movement within biofilms, further leveraging amplified copper ion interference and macrophage reprogramming to eradicate refractory orthopedic IABIs.

Recently, nanoscale metal peroxides comprising metal ions and peroxo groups, have emerged as effective sources of H_2O_2 for antibacterial applications[22,39]. Among the Fenton-like metal peroxide enzymes, CP nanodots uniquely provide H_2O_2 and Fenton-type copper(II), enabling self-supplying chemodynamic therapy (Fig. 2e). The utilization of metal peroxides significantly enhances the efficacy of therapies that rely on ROS. Transmission Electron Microscopy (TEM) image and size distribution analysis confirmed the successful synthesis of CP nanodots, which exhibited a remarkably uniform size of approximately 5 nm (Fig. 2f). A colorimetric assay demonstrated that H_2O_2 released from CP caused the discoloration of $KMnO_4$ (from purple to colorless) via a redox reaction (Fig. 2g). Similarly, the capability of CP to generate •OH radicals was evidenced by an absorption peak at 650 nm, corresponding to the oxidation of TMB and the resulting color change (Fig. 2h). X-ray photoelectron spectroscopy (XPS) analysis was conducted on CP and CP + NIR to evaluate the valence state changes of copper ions in CP. The results showed that the Cu 2*p* XPS spectra of CP featured two primary peaks at 932.8 and

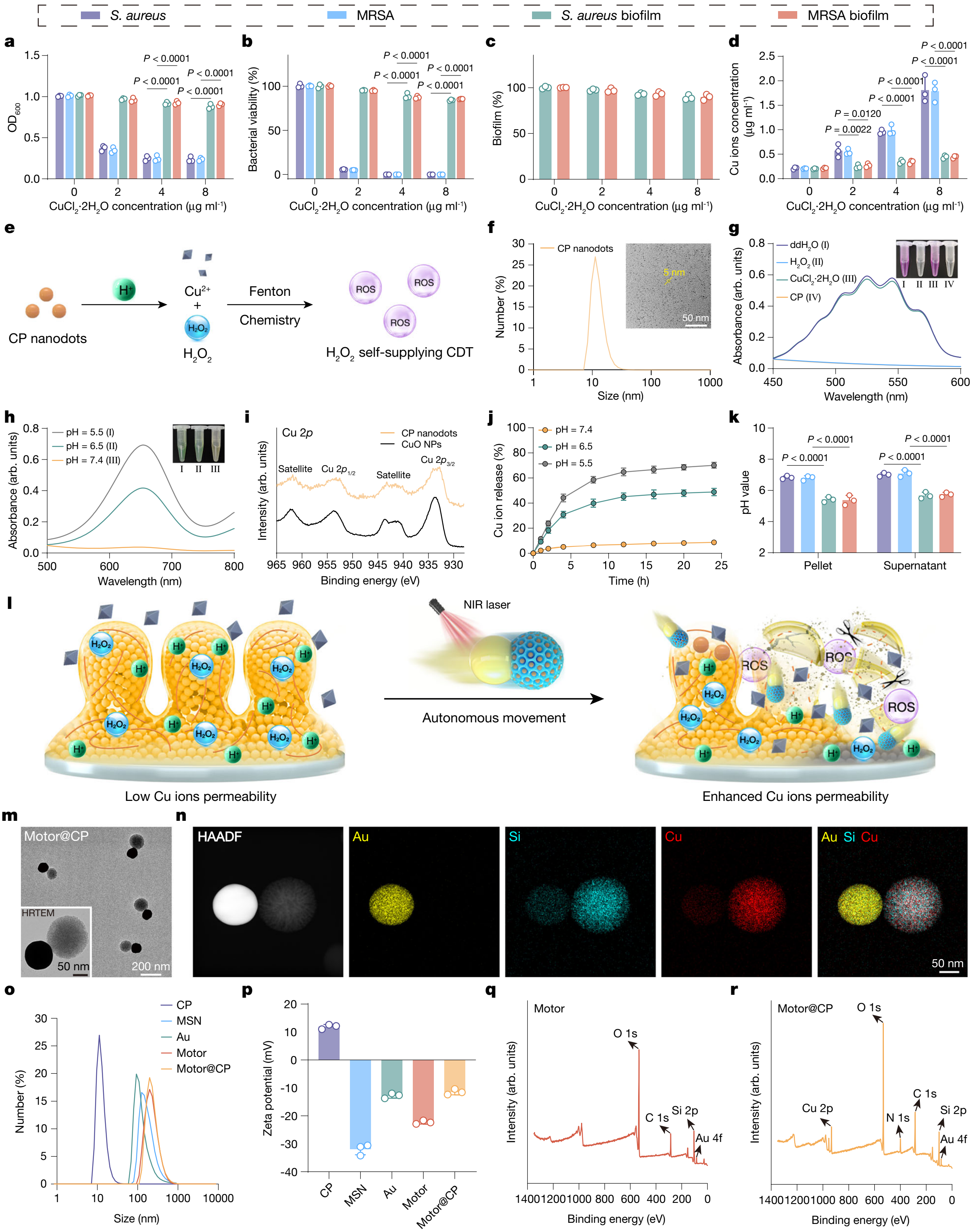

953.2 eV, along with satellite peaks at 943.2 and 961.8 eV (Fig. 2i). For CP + NIR, the Cu 2*p* XPS spectra exhibited two main peaks at 933.1 and 953.4 eV, accompanied by satellite peaks at 943.3 and 962.1 eV. These findings confirm that the copper in CP nanodots remains in the +2 valence state, indicating that NIR irradiation does not alter the valence state of copper ions in CP (Supplementary Fig. 3). The release of copper ions from CP was systematically monitored over 24 h in phosphate-buffered saline (PBS) at varying pH levels (7.4, 6.5, and 5.5). The results clearly demonstrated the acid-responsive nature of copper ion release by CP (Fig. 2j). To more accurately assess the self-supplying H_2O_2 capacity of CP, the H_2O_2 level was continuously monitored over a 24 h period. The results revealed that CP is capable of generating sustained H_2O_2 production (achieving 69.9 ± 4.3% within 12 h), thereby creating favorable conditions for enhancing the Fenton-like reaction

Fig. 2 | In vitro antibiofilm activities of two copper ion donors against *S. aureus*, planktonic MRSA, and biofilms, as well as the characterization of CP and Motor@CP. a The OD_{600} values of *S. aureus*, MRSA planktons, and biofilms were measured after incubation with different concentrations of $CuCl_2·2H_2O$. Data are presented as mean ± s.d. (*n* = 3 biologically independent samples). **b** The viability of *S. aureus*, MRSA planktons, and biofilms was assessed at varying concentrations of $CuCl_2·2H_2O$ using SPM. Data are presented as mean ± s.d. (*n* = 3 biologically independent samples). **c** Quantification of the biomass of *S. aureus* and MRSA biofilms with different concentrations of $CuCl_2·2H_2O$ by crystal violet assay. Data are presented as mean ± s.d. (*n* = 3 biologically independent samples). **d** Intracellular copper concentrations were determined via ICP-OES. Data are presented as mean ± s.d. (*n* = 3 biologically independent samples). **e** Schematic diagram of Fenton-like catalytic kinetics of CP. **f** The hydrodynamic diameter of CP and its representative TEM image. **g** $KMnO_4$ assay was performed to detect peroxide groups. **h** TMB assay was used to assess •OH generation in PBS at pH 5.5, 6.5, and 7.4. **i** Cu 2*p* XPS spectra of CP nanodots and CuO NPs. **j** Cu ions release rates of CP in different PBS (pH 7.4, 6.5, and 5.5). Data are presented as the mean ± s.d. (*n* = 3 biologically independent samples). **k** pH values of the pellet and supernatant from *S. aureus*, MRSA planktonic culture systems, and biofilm medium were recorded. Data are presented as mean ± s.d. (*n* = 3 biologically independent samples). **l** Schematic illustration of an autonomously moving nanomotor for biofilm penetration to increase the action of copper ions. **m** TEM and HRTEM images of Motor@CP. **n** Element mapping images of Motor@CP. **o**, **p** Hydrodynamic diameter distribution and zeta potential values of CP, MSN, Au, Motor, and Motor@CP. Data are presented as mean ± s.d. (*n* = 3 biologically independent samples). **q**, **r** Survey XPS spectra of Motor and Motor@CP. Statistical significance was assessed using two-way ANOVA with Tukey's multiple comparison test.

and ensuring sufficient ROS generation (Supplementary Fig. 4). Additionally, the chemical properties of the BME were analyzed to determine optimal conditions for CP-BME interactions. The biofilm pellets in *S. aureus* and MRSA cultures exhibited a low pH (Fig. 2k), creating an acidic environment conducive to the generation of H_2O_2, copper(II), and toxic •OH by CP nanodots.

Subsequently, the aforementioned routine antibiofilm experiments were conducted in *S. aureus* and MRSA biofilms. The results demonstrated that CP outperformed $CuCl_2·2H_2O$ in biofilm eradication (Supplementary Figs. 5–7). ICP-OES analysis further confirmed that CP treatment resulted in an increase in copper content within both *S. aureus* and MRSA biofilms (Supplementary Fig. 7d), attributed to CP's self-supplying H_2O_2 capacity, which enhances ROS production and interferes with copper ion uptake and efflux channels. Compared with traditional copper ion donor, these findings highlight the potential of CP to promote intracellular copper accumulation in biofilm infections. The in vitro cytotoxicity of various concentrations of CP nanodots on L929 cells, RAW 264.7 cells, and HUVEC cells was evaluated using the CCK-8 assay. It was determined that a concentration of 4 μg ml^{-1} represents the optimal antibiofilm concentration while exhibiting negligible cytotoxic effects on normal cells (Supplementary Fig. 8a–c). Although CP is capable of providing copper ions within an appropriate range; its passive nanoparticle action mode exhibits limited penetration efficacy against dense biofilms, necessitating further investigation into strategies to enhance its biofilm-penetrating capability.

Owing to the superior and controllable autonomous motion, nanomotors hold promise in overcoming dense biofilm barriers, diffusing extensively within biofilms, and maximizing the antibiofilm effect through effective delivery of copper ions within a safe concentration range (Fig. 2l). In this study, MSNs were chosen as the nanomotor carrier due to their high loading capacity and biocompatibility, while AuNPs were utilized as propulsion components for their outstanding photothermal conversion efficiency. TEM images revealed that MSNs exhibited monodispersity with central radial structures, and AuNPs displayed similarly spherical shapes with smooth surfaces (Supplementary Figs. 9 and 10). Nitrogen absorption-desorption tests and Brunauer-Emmett-Teller analysis indicated an average pore size of 10.1 nm for MSNs, confirming the feasibility of loading CP nanodots into MSNs (Supplementary Fig. 11a, b). The Pickering emulsion method was employed to incorporate MSNs into paraffin wax, demonstrating a promising technique for the formation of *Janus* particles[40]. Scanning electron microscope (SEM) images showed a monolayer of MSNs anchored on paraffin wax (Supplementary Fig. 12). To achieve precise fabrication of *Janus* bisphere structures, various mass ratios of MSN to AuNPs (1:1, 1:1.5, and 1:2) were tested to identify the optimal combination. TEM images confirmed the successful attachment of AuNPs to one side of MSNs, forming the optimal *Janus* bisphere MSN-Au (Motor) structure at a mass ratio of 1:1.5 (Supplementary Fig. 13). Our preparation method ensured excellent uniformity of the *Janus* bisphere Motor (Supplementary Fig. 14). Subsequently, CP nanodots were encapsulated within the nanomotor to fabricate the Motor@CP structure. High-resolution transmission electron microscopy (HRTEM) images revealed that MSN exhibited a regular aperture structure before CP loading, however, this regular structure was no longer observable after CP encapsulation (Fig. 3m and Supplementary Fig. 15). Elemental mapping images confirmed the successful synthesis of the Motor@CP *Janus* bisphere, characterized by a large and uniform distribution of copper elements on the MSN side (Fig. 3n). DLS measurements were then performed on various nanomaterials, including MSN, AuNPs, Motor, and Motor@CP, to evaluate their size distributions. The hydrodynamic sizes of all sample was similar, with the addition of CP causing a slight increase in particle size compared to the Motor alone (Fig. 3o). Zeta potential measurements further corroborated the successful formation of Motor@CP. The zeta potential values for MSN and AuNPs were −31.9 ± 2.0 mV and −12.8 ± 0.9 mV, respectively. In contrast, the negative surface charge of Motor and Motor@CP decreased to −22.3 ± 0.6 mV and −11.4 ± 1.0 mV, respectively (Fig. 3p). Additionally, XPS detection was conducted to evaluate the Motor and Motor @CP (Fig. 3q, r). Compared with the spectrum of pristine Motor, the survey spectrum showed an obvious characteristic peak of Cu 2*p*, while the high-resolution spectrum of Cu 2*p* showed two deconvolved peaks at 932.9 and 952.5 eV, confirming the successful formation of Motor@CP (Supplementary Fig. 16). The self-supplying H_2O_2 capability of Motor@CP was further investigated. The release of H_2O_2 was continuously monitored over a 24 h period, and the results demonstrated that Motor@CP could sustainably produce H_2O_2, achieving a release rate of 69.4 ± 5.2% within 12 h (Supplementary Fig. 17). Electron spin resonance (ESR) analysis also confirmed the ability of Motor@CP to generate •OH radicals in an acidic environment (Supplementary Fig. 18). Collectively, these results demonstrate successful loading of CP. The high nanoparticle-loading capacity of MSN enabled the CP-loading efficiency of the *Janus* bisphere nanomotors to reach 12.5 ± 0.7%.

Movement performance and biofilm penetration behavior of Motor@CP

Leveraging asymmetric absorption of NIR light, our *Janus* bisphere nanomotors Motor@CP were capable of generating self-thermophoretic propulsion (Fig. 3a). Initially, we monitored temperature changes in aqueous solutions containing Motor@CP under varying NIR laser irradiation intensities. The results demonstrated that the solution temperature increased proportionally with the intensity of the NIR laser, achieving a photothermal conversion efficiency of ~30.6% (Fig. 3b and Supplementary Fig. 19). Representative tracking trajectories of Motor@CP in PBS solution (pH 7.4) were observed at different NIR laser power intensities (Fig. 3c and Supplementary Fig. 20). Notably, the movement distance of Motor@CP progressively increased as the NIR laser power was elevated.

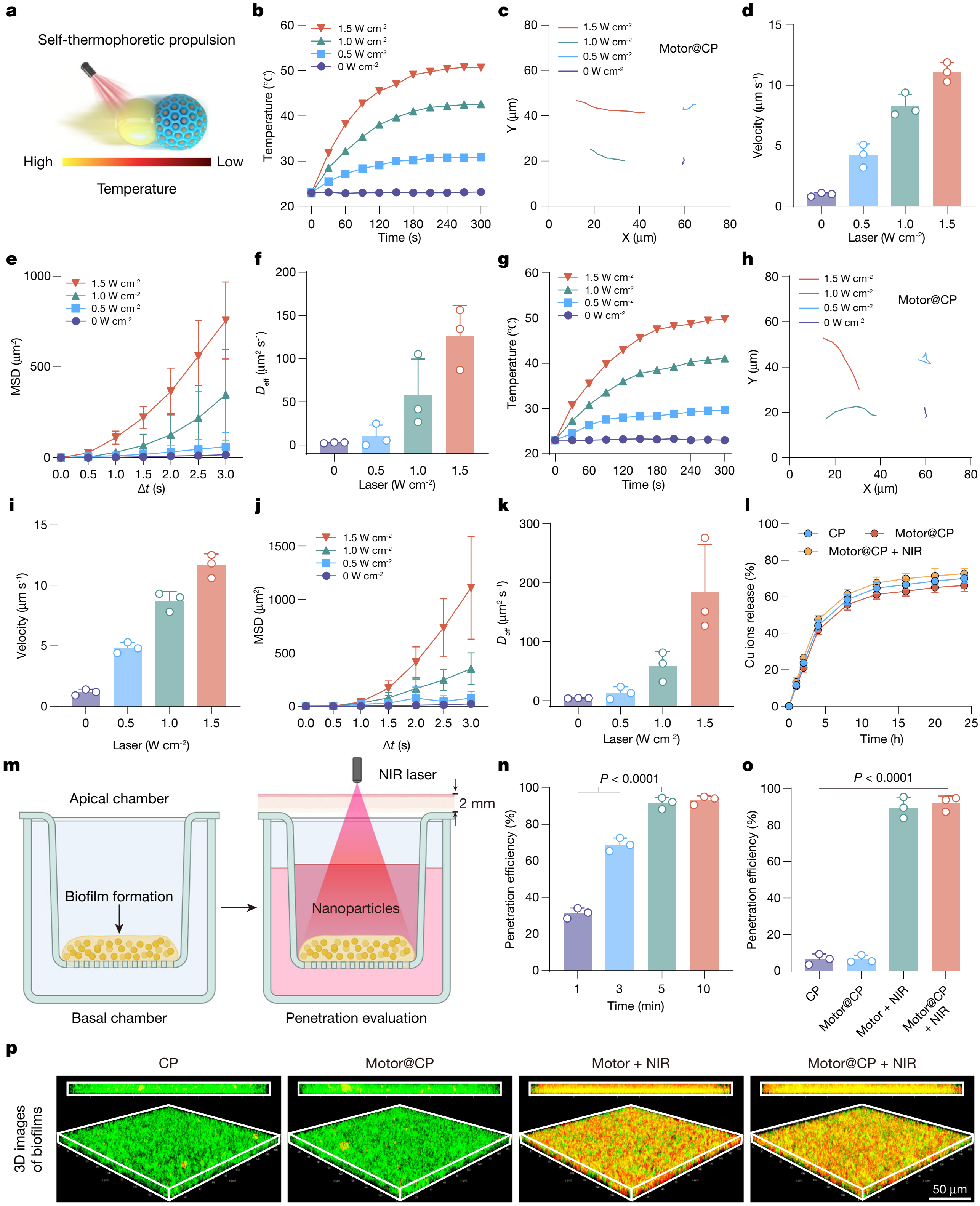

Specifically, under no NIR laser irradiation (0 W cm^{-2}), the motion was irregular, under low-intensity irradiation (0.5 W cm^{-2}), the motion appeared relatively random (Supplementary Movie 1). In contrast, Motor@CP with the *Janus* bisphere structure exhibited more directional movement under higher NIR laser powers (1.0 and 1.5 W cm^{-2}). The velocities of Motor@CP under different NIR laser irradiations (0.5, 1.0, and 1.5 W cm^{-2}) were 4.2 ± 0.9 μm s^{-1}, 8.3 ± 0.9 μm s^{-1}, and 11.1 ± 0.8 μm s^{-1}, respectively (Fig. 3d). Additionally, as the laser power increased, both the mean square displacement (MSD) and the corresponding effective diffusion coefficient (D_{eff}) of Motor@CP showed significant increases (Fig. 3e, f).

To mimic subcutaneous acidic biofilm microenvironments, we further evaluated the motor performance in acidic PBS (pH 5.5)

Fig. 3 | In vitro movement and biofilm penetration performance of Motor@CP. **a** Schematic illustration of the movement of NIR laser-driven Motor@CP. **b** Temperature elevation of Motor@CP in PBS (pH 7.4) with different NIR laser power (0, 0.5, 1.0, and 1.5 W cm^{-2}). **c** Representative tracking trajectories of Motor@CP in PBS (pH 7.4) with different NIR laser power (0, 0.5, 1.0, and 1.5 W cm^{-2}) over 3 s. **d**–**f** Velocity, MSD curve, and corresponding D_{eff} of Motor@CP in PBS (pH 7.4) under different NIR laser power. Data are presented as mean ± s.d. ($n = 3$ biologically independent samples). **g** Temperature elevation of Motor@CP in PBS (pH 5.5) with different NIR laser power (0, 0.5, 1.0, and 1.5 W cm^{-2}). **h** Representative tracking trajectories of Motor@CP in PBS (pH 5.5) with different NIR laser power (0, 0.5, 1.0, and 1.5 W cm^{-2}) over 3 s. **i**–**k** Velocity, MSD curve, and D_{eff} of Motor@CP in PBS (pH 5.5) under different NIR laser power. Data are presented as mean ± s.d. ($n = 3$ biologically independent samples). **l** Cu ions release rates of CP, Motor@CP, and Motor@CP + NIR in PBS (pH 5.5). Data are presented as mean ± s.d. ($n = 3$ biologically independent samples). **m** Schematic diagram of transwell assay composed of *S. aureus* biofilm. Created in BioRender. Liuliang He (2025) (https://BioRender.com/ov97w82). **n** The ratio of Motor@CP penetrated into basal chamber after different time (1, 3, 5, and 10 min) of NIR laser irradiation in apical chamber. Data are presented as mean ± s.d. ($n = 3$ biologically independent samples). **o** The ratio of nanoparticles penetrated into basal chamber after 5 min of incubation in apical chamber. Data are presented as mean ± s.d. ($n = 3$ biologically independent samples). **p** 3D CLSM images and corresponding z-stack fluorescent images of nanoparticles penetrating *S. aureus* biofilm for 5 min. Green: live bacteria, Red: rhodamine B labeled nanoparticles. These experiments (**g**–**k**, **m**–**o**) were covered by a slice of 2.0 mm-thick pork ham. Statistical significance was assessed using one-way ANOVA with Tukey's multiple comparison test.

covered by a 2.0 mm-thick slice of pork ham[41,42]. The temperature increase of Motor@CP was proportional to the increase in NIR laser power (Fig. 3g). Representative tracking trajectories under varying NIR laser powers were shown in Fig. 3h, Supplementary Fig. 21, and Supplementary Movie 2. As the NIR laser power increased in acidic solution (0.5, 1.0, and 1.5 W cm^{-2}), the velocity of Motor@CP was caculated as 4.8 ± 0.4 μm s^{-1}, 8.7 ± 0.6 μm s^{-1}, and 11.6 ± 0.8 μm s^{-1}, respectively (Fig. 3i), and the corresponding MSD and D_{eff} also exhibited significant increases (Fig. 3j, k). This superior self-thermophoretic capability may facilitate more efficient penetration into biofilms for copper ions delivery. The release behavior of copper ions from CP after loading was evaluated using ICP-OES. Within 24 h in PBS (pH 5.5), the copper ion release ratios of CP, Motor@CP and Motor@CP + NIR (4 μg ml^{-1}, expressed in terms of CP) were 70.1 ± 2.2%, 66.3 ± 3.4% and 72.6 ± 3.0% respectively (Fig. 3l), with actual copper ion concentrations of 1.362 ± 0.043, 1.287 ± 0.067 and 1.412 ± 0.052 ug ml^{-1} respectively (Supplementary Fig. 22). This implies that Motor@CP + NIR achieves a more efficient antibiofilm effect through autonomous nanomotor movement and ROS generation at lower copper ion concentrations. Efficient nanoparticle penetration through the dense protective layer of biofilms is critical for disrupting biofilm integrity and effectively eliminating bacteria via copper ion release. Therefore, this study evaluated the penetration properties into biofilms of different nanoparticles by co-incubating them with biofilms. Prior to this, the biocompatibility of the samples was assessed through hemolysis and cytotoxicity assays conducted in vitro. The hemolysis ratio for all samples was below 5%, comparable to the negative control (PBS solution), indicating excellent hemocompatibility (Supplementary Fig. 23). Additionally, we assessed in vitro biocompatibility under varying concentration and NIR laser power intensities using the CCK-8 assay. After 24 h co-culture with L929 cells, RAW 264.7 cells, and HUVEC cells, Motor@CP + NIR demonstrated excellent biocompatibility at the concentration (4 μg ml^{-1}, expressed in terms of CP) (Supplementary Fig. 24). In subsequent experiments, we employed a NIR laser power of 1.0 W cm^{-2}, as this power level enabled Motor@CP to exhibit superior motility performance while exerting negligible cytotoxic effects (Supplementary Fig. 25).

Subsequently, to simulate realistic conditions of subcutaneous biofilm infections, the transwell system was employed to quantify the penetration capability (Fig. 3m and Supplementary Fig. 26). *S. aureus* biofilm was established in the apical chamber, and rhodamine B-labeled fluorescent nanoparticles were introduced into this chamber, with a 2.0 mm thick pork ham slice covering the surface. The penetration efficiency of Motor@CP through the biofilm was evaluated under varying durations of NIR laser irradiation. Prolonged laser exposure significantly enhanced the penetration efficacy of Motor@CP (Fig. 3n), achieving near-optimal efficiency (>90%) after 5 min of irradiation. Additionally, irradiation for 10 min demonstrated no significant increase in penetration efficiency, while prolonged irradiation may result in undesirable tissue heat damage. Therefore, we selected a laser irradiation time of 5 min in the whole experiment. Furthermore, the biofilm penetration efficiencies of different nanoparticles were compared by measuring the fluorescence intensity in the basal chamber after 5 min of laser irradiation. The results demonstrated that the biofilm penetration ratio of Motor@CP + NIR was 14.2-fold higher than that of the CP group (Fig. 3o), highlighting the exceptional potential of Motor@CP + NIR with autonomous motion in penetrating biofilms. 3D confocal laser scanning microscopy (CLSM) was further performed following the incubation of rhodamine B-labeled nanoparticles with *S. aureus* and *E. coli* biofilms. The results demonstrated that Motor@CP + NIR exhibited robust penetration into both *S. aureus* and *E. coli* biofilms (Fig. 3p and Supplementary Figs. 27 and 28). In contrast, negligible penetration was observed in the CP group alone. These findings suggest that the self-thermophoretic propulsion of Motor@CP + NIR significantly enhanced biofilm penetration and exhibited broad-spectrum applicability to different biofilms.

In vitro antibiofilm activity of Motor@CP

Representatives of Gram-positive (*S. aureus* and MRSA) and Gram-negative (*E. coli*) bacteria were selected as model biofilm-forming organisms to investigate the in vitro antibiofilm activity of Motor@CP. These bacteria were cultured for 3 days to establish stable biofilms, followed by different treatments, including Control (untreated), CP, Motor, Motor@CP, and Motor@CP + NIR, to validate their therapeutic effects on biofilm eradication. After a 12 h co-incubation period with established biofilms, the Motor@CP + NIR group exhibited a significant reduction in OD_{600} values for *S. aureus*, MRSA, and *E. coli* biofilms (Supplementary Fig. 29a–c). Crystal violet staining revealed that while the Control and Motor groups maintained intact biofilm structures, the CP and Motor@CP treatment groups showed biofilms with partial structural damage but largely preserved viability (Fig. 4a–c and Supplementary Fig. 30a, b). Spread plate method (SPM) analysis further confirmed a marked decrease in bacterial presence within the biofilm in the Motor@CP + NIR treatment group, and colony-forming unit (CFU) analysis demonstrated that the Motor@CP + NIR treatment achieved a 99.9% bacterial clearance rate, indicating superior inhibition of bacterial growth and biofilm formation (Fig. 4d–f and Supplementary Figs. 31a, b). This clearance rate was significantly higher compared to any other treatment groups, confirming that Motor@CP + NIR provided the most potent disruption of the biofilm. 3D CLSM images of *S. aureus* and MRSA biofilms were utilized to assess the extent of biofilm disruption. In the Motor@CP + NIR group, a pronounced disruption of the biofilm architecture was observed, characterized by intense red fluorescence, which strongly indicated a high degree of bacterial cell death. This finding underscores the efficacy of the treatment in compromising the biofilm structure (Fig. 4g). Furthermore, SEM images (Fig. 4h and Supplementary Fig. 32) revealed dense bacterial colonies with intact morphology in the Control, CP, Motor, and Motor@CP groups. Conversely, bacteria within the biofilms treated with Motor@CP + NIR exhibited predominantly shriveled, distorted, or fully lysed cells, thereby confirming the treatment's

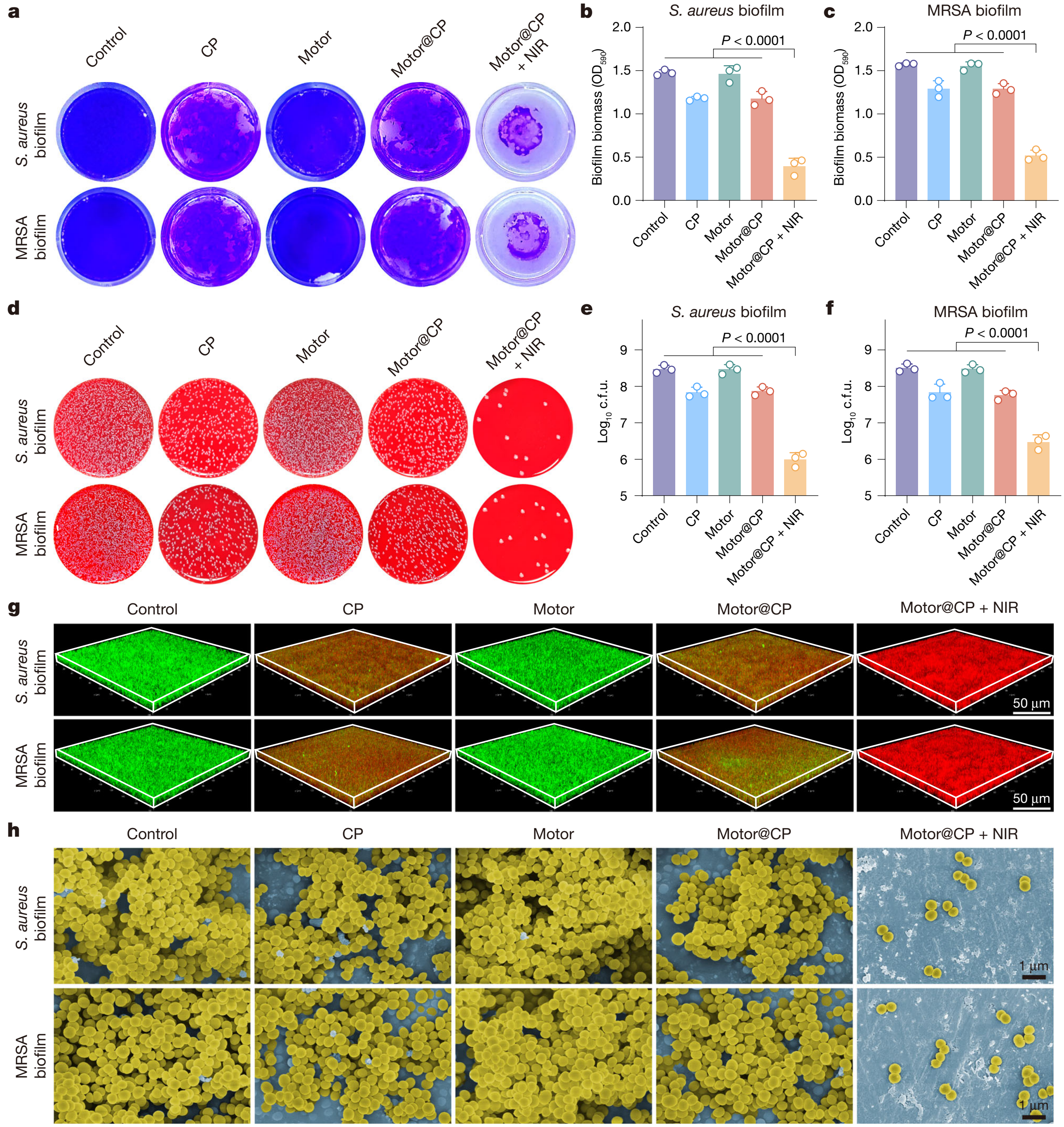

Fig. 4 | In vitro antibiofilm activity of Motor@CP. a Representative crystal violet staining images of *S. aureus* and MRSA biofilms in the Control, CP, Motor, Motor@CP, and Motor@CP + NIR treatment groups. **b**, **c** Quantitative analysis of the biomass of *S. aureus* and MRSA biofilms after different treatments. Data are presented as mean ± s.d. ($n = 3$ biologically independent samples). **d** Representative images of colonies derived from *S. aureus* and MRSA biofilms in the aforementioned treatment groups. **e**, **f** CFU counts for *S. aureus* and MRSA biofilms after different treatments was determined using SPM. Data are presented as mean ± s.d. ($n = 3$ biologically independent samples). **g** 3D CLSM images of *S. aureus* and MRSA biofilms stained with SYTO9 (green: live bacteria) and PI (red: dead bacteria) to visualize biofilm disruption. **h** SEM images of *S. aureus* and MRSA biofilms following treatment with different groups. Statistical significance was assessed using one-way ANOVA with Tukey's multiple comparison test.

effectiveness in biofilm eradication. The photothermal effect of AuNPs was investigated separately, and the results indicated that at a power of 1.0 W cm^{-2}, the photothermal effect of AuNPs alone on the biofilms was negligible (Supplementary Figs. 33–35). Collectively, these results suggest that single-ion therapy (CP or Motor@CP groups) exhibits moderate antibiofilm activity, while the Motor@CP + NIR group demonstrates superior efficacy in eliminating biofilms in vitro through the utilization of self-thermophoretic nanomotors.

Antibacterial mechanism of Motor@CP

Bio-TEM was employed to investigate the ultrastructure and intracellular copper ion uptake of *S. aureus* and *E. coli* following diverse treatment. The *S. aureus* and *E. coli* exposed to Motor@CP + NIR exhibited more pronounced structural disruptions. Further elemental mapping analysis revealed a significantly higher intracellular copper concentration in the Motor@CP + NIR group compared to the CP group, indicating enhanced copper ion internalization (Fig. 5a and

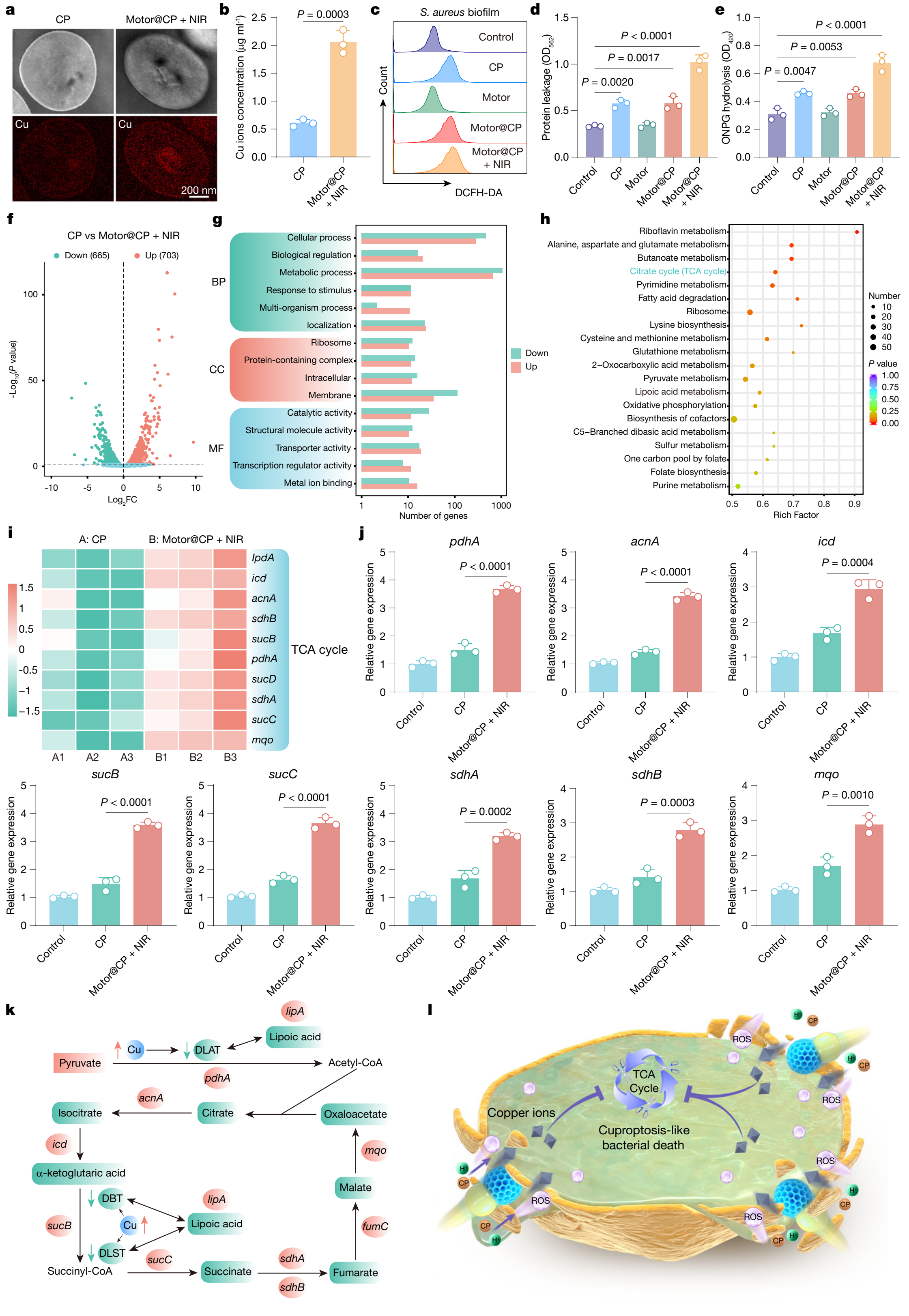

Supplementary Fig. 36). To quantify this observation, ICP-OES analysis was performed. The results demonstrated that the intracellular copper levels of *S. aureus* and *E. coli* treated with Motor@CP + NIR increased significantly by 3.4- and 4.1-fold respectively, confirming substantial copper ion influx (Fig. 5b and Supplementary Fig. 37). This enhanced copper uptake can be attributed to the synergistic effect of autonomous movement and ROS generation, leading to increased membrane permeability (Fig. 5c and Supplementary Figs. 38–40). Extracellular DNA (eDNA) plays a critical role in the formation, maturation and structural stability of biofilms[43,44]. Through SYTOX green nucleic acid staining of eDNA in *S. aureus* and *E. coli* biofilms, the results indicated that Motor@CP + NIR group exhibited superior eDNA degradation within the biofilm. This is due to the autonomous movement enabling penetration of the biofilm structure and simultaneous delivery of CP to

Fig. 5 | In vitro antibacterial mechanism of Motor@CP. a Microstructural analysis and element mapping of copper ions in *S. aureus* using Bio-TEM. **b** Intracellular copper ions concentration within *S. aureus* biofilm measured by ICP-OES. Data are presented as the mean ± s.d. ($n = 3$ biologically independent samples). **c** Flow cytometry results of ROS levels in *S. aureus* biofilm measured by DCFH-DA. **d** Protein leakage of *S. aureus* biofilm after various treatments calculated by BCA assay. Data are presented as the mean ± s.d. ($n = 3$ biologically independent samples). **e** Membrane permeability of *S. aureus* biofilm after various treatments evaluated with ONPG hydrolysis assay. Data are presented as the mean ± s.d. ($n = 3$ biologically independent samples). **f** Volcano plot depicting the DEGs in the comparison of Motor@CP + NIR versus CP is presented. Statistical significance was determined using a two-tailed *t*-test. Genes with an adjusted $P < 0.05$ are displayed in red or green dots ($n = 3$). FC, fold change. **g** GO annotation chart of DEGs (BP biological process, CC cellular component, MF molecular function). **h** KEGG enrichment analysis of the top 20 relevant pathways in response to Motor@CP + NIR compared with CP ($n = 3$). Statistical significance was determined using a two-tailed *t*-test. The *y*-axis represents significantly enriched KEGG pathways, while the *x*-axis corresponds to their respective enrichment factors. The color indicates the degree of enrichment significance (*P* value). **i** Heatmap cluster analysis of DEGs involved in the bacterial TCA cycle based on expression patterns. **j** In vitro qPCR analysis for the relative gene expression of TCA cycle pathway. Data are presented as the mean ± s.d. ($n = 3$ biologically independent samples). **k**, **l** Schematic diagram of the mechanism analysis between differential metabolites and differentially expressed genes. Red rectangles represent increased metabolites, while green rectangles represent decreased metabolites. Red circles indicate up-regulated genes, and green ovals indicate down-regulated genes. DLAT Dihydrolipoamide S-Acetyltransferase. DBT Dihydrolipoamide Branched Chain Transacylase E2. DLST Dihydrolipoamide S-Succinyltransferase. Statistical significance was assessed using two-tailed unpaired *t*-test (**b**) and one-way (**d**, **e**, **j**) ANOVA with Tukey's multiple comparison test.

disrupt the eDNA component (Supplementary Figs. 41 and 42). Additionally, protein leakage assays and O-nitrophenyl β-D-galactopyranoside (ONPG) hydrolysis assays were conducted to evaluate bacterial content leakage, providing further evidence for the damaged membrane integrity (Fig. 5d, e and Supplementary Fig. 43a, b). These findings strongly support the conclusion that Motor@CP + NIR treatment significantly compromises the intergrity and alters the permeability of *S. aureus* and *E. coli* biofilm and bacterial membranes, resulting in evident cytoplasmic leakage.

Encouraged by the above findings, we conducted an in-depth investigation into the germicidal mechanism using RNA-seq analysis of *S. aureus* to compare differentially expressed genes (DEGs) between CP and Motor@CP + NIR groups. Principal component analysis and heatmap correlation analysis (Supplementary Figs. 44, 45) revealed significant expression differences while demonstrating minimal variability within each group, thereby validating the reliability of our RNA-seq data. A total of 3,043 variables were identified, with 703 genes significantly upregulated and 665 genes downregulated in the Motor@CP + NIR group relative to the CP group (Fig. 5f). Gene Ontology (GO) enrichment analysis indicated that the disruption primarily affected bacterial cellular metabolism and catalytic activities, specifically impacting the metabolism of peptides, proteins, amides, and macromolecules (Fig. 5g). This suggests a substantial alteration in bacterial metabolic pathways and enzymatic functions critical for maintaining cellular homeostasis and macromolecule synthesis. Kyoto Encyclopedia of Genes and Genomes (KEGG) enrichment analysis of DEGs revealed that Motor@CP + NIR treatment significantly inhibited *S. aureus* in key pathways such as the citrate cycle (TCA), ribosome, pyrimidine metabolism, riboflavin metabolism, and several amino acid metabolism pathways, as shown in the top 20 enriched metabolic pathways (Fig. 5h). Notably, the TCA cycle was particularly impacted, with a high enrichment index and low *p* value, providing compelling evidence for a cuproptosis-like death mechanism. Cuproptosis, a recently identified form of cell death induced by copper ions, leads to the accumulation of four enzymes associated with lipoic acid in the TCA cycle, thereby disrupting the activity of iron-sulfur (Fe-S) cluster proteins. Intriguingly, our analysis demonstrated that Motor@CP + NIR treatment resulted in the upregulation or downregulation of genes related to a bacterial cuproptosis-like phenomenon (Fig. 5i and Supplementary Fig. 46). This suggests that the treatment can induce a copper-dependent form of bacterial death, analogous to the process observed in eukaryotic cells.

To more clearly elucidate the mechanism, we conducted qPCR assays to validate the levels of relevant genes and metabolites in the TCA cycle. The quantitative results demonstrated that the Motor@CP + NIR group exhibited the highest levels of related genes and the lowest levels of metabolites compared to the Control and CP groups (Fig. 5j and Supplementary Fig. 47). Schematic diagram of the mechanism analysis between vividly illustrated the changes in TCA cycle metabolites and the differentially expressed genes influenced by them (Fig. 5k, l). Collectively, under the influence of ROS, bacteria treated with Motor@CP + NIR showed increased intracellular copper, which bound to fatty acylases (DLAT, DBT, and DLST)[14,45], leading to their inactivation and subsequent reduction of metabolites throughout the pathway. Additionally, lipoic acid was reduced due to the formation of more lipoacylated proteins[46], resulting in up-regulation of genes regulating lipoic acid synthesis[47]. Ultimately, the reduced metabolites were regulated by negative feedback, increasing the expression of genes that regulate the TCA cycle. In summary, through effective biofilm penetration, autonomous intrabiofilm delivery, and the generation of •OH from CP in the acidic BME, Motor@CP + NIR treatment enhances intracellular copper(II) uptake and disrupts the TCA cycle, ultimately leading to a cuproptosis-like death in bacteria.

In vivo antibiofilm activity of Motor@CP

Building on the well-documented biofilm elimination capabilities and characterized mechanism of Motor@CP, we conducted an in-depth evaluation of its antibiofilm activity in vivo using a murine model of IABIs[48]. The detailed procedure and timeline was shown in Fig. 6a. Specifically, prior to implantation, bacterial suspension (10^6 CFU ml^{-1}) was co-cultured with the PEEK implant for 3 days to induce the formation of bacterial biofilm. Subsequently, the biomass of the formed biofilm was quantitatively assessed using crystal violet staining (Supplementary Fig. 48a, b), while the morphology and thickness of biofilm on the PEEK surface were evaluated via SEM (Supplementary Fig. 48c). The results demonstrated a well-developed and dense biofilm was successfully formed on the PEEK surface. Throughout the 10-day treatment period, the skin tissue surrounding the subcutaneous implants was continuously monitored (Fig. 6b). The Control and Motor groups exhibited pronounced signs of inflammation, including swelling, pus formation, and even implant exposure or shedding, indicative of a biofilm-induced inflammatory response at the infection site. The CP and Motor@CP groups showed moderate inflammatory signs, while the Motor@CP + NIR group displayed only mild swelling, minimal pus, or wound festering. Notably, by day 6 post-operation, the infected area in the Motor@CP + NIR group showed a significant reduction, with a consistent decline observed in subsequent days (Fig. 6c), demonstrating superior in vivo antibiofilm activity compared to the other treatment groups. Although initial body weight loss was noted due to infection, mice in the Motor@CP + NIR group began to regain weight by day 4 (Fig. 6d).

Following various treatments, the bacterial residue on inserted implants and infiltration in surrounding tissues were quantitatively assessed by determining the CFU count. SPM results indicated stable colony counts in both the Control and Motor groups, suggesting minimal impact on bacterial viability (Fig. 6e, f). In contrast, a modest decrease in CFU counts was observed in the CP and Motor@CP groups, indicating some reduction in bacterial presence. The most

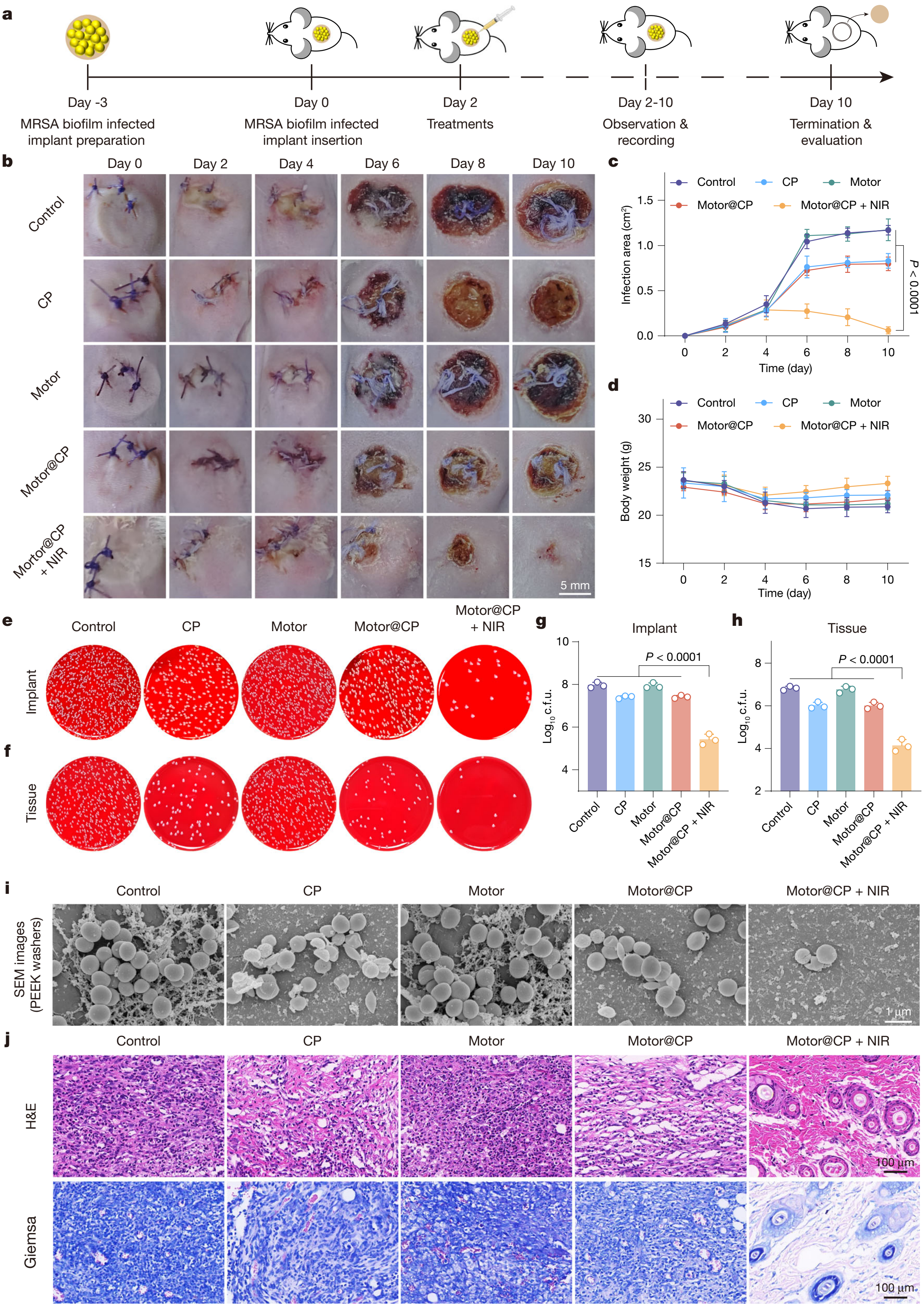

Fig. 6 | Evaluation of the in vivo therapeutic effect in the implant-associated biofilm infection model. **a** Schematic illustration of the treatment procedure used in the implant-associated MRSA biofilm infection model study. **b** Macroscopic images of the wound sites following different treatments ($n = 5$ biologically independent samples). **c** Infection area progression curves showing the average infection size after various treatments. Data are presented as the mean ± s.d. ($n = 3$ biologically independent samples). **d** Body weight changes of the mice throughout the in vivo experiment. Data are presented as the mean ± s.d. ($n = 3$ biologically independent samples). **e** Representative colony images of PEEK using SPM. **f** Representative colony images of peripheral tissue using SPM. **g**, **h** CFU counts corresponding to the SPM results for PEEK and peripheral tissue. Data are presented as the mean ± s.d. ($n = 3$ biologically independent samples). **i** SEM images of PEEK washers collected from each group. **j** H&E and Giemsa staining of peripheral tissues following different treatments. Statistical significance was assessed using one-way (**g**, **h**) and two-way (**c**) ANOVA with Tukey's multiple comparison test.

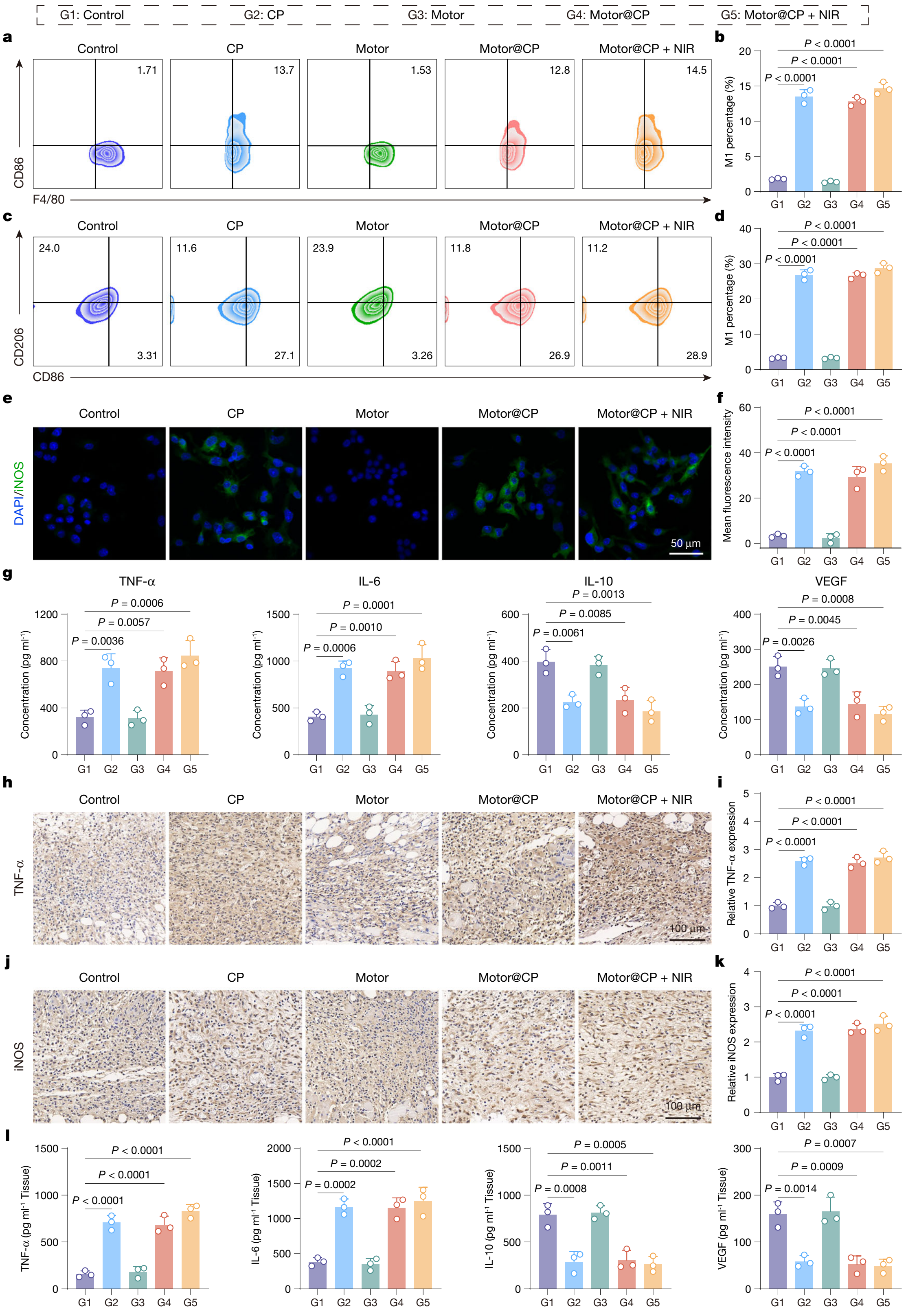

significant reduction in bacterial load was noted in the Motor@CP + NIR group, where CFU counts were markedly lower, highlighting the superior antibiofilm efficacy of this treatment (Fig. 6g, h). These findings were corroborated by SEM images (Fig. 6i), which demonstrated a clear correlation with the SPM data. In the Motor@CP + NIR group, the majority of bacteria appeared dead and fragmented, with a significant reduction in intact, viable bacterial cells. This comprehensive analysis underscores the potent antibiofilm efficacy of the Motor@CP + NIR treatment. Histomorphological and quantitative analyses were performed on peripheral tissues from the infection sites. Hematoxylin and eosin (H&E) staining revealed substantial neutrophil infiltration in the Control, CP, Motor, and Motor@CP groups, indicative of a pronounced inflammatory response associated with infection. Conversely, inflammation was markedly reduced and effectively controlled

Fig. 7 | Evaluation of immunomodulatory capability in vitro and in vivo. **a**, **b** Representative flow cytometry and corresponding quantification of M0-M1 macrophages in vitro showed changes in CD86 and F4/80 expression in RAW 264.7 macrophages after different treatments. Data are presented as mean ± s.d. (*n* = 3 biologically independent samples). **c**, **d** Representative flow cytometry and corresponding quantification of M2-M1 macrophages in vitro showed changes in CD86 and CD206 expression in RAW 264.7 macrophages after different treatments. Data are presented as mean ± s.d. (*n* = 3 biologically independent samples). **e**, **f** Immunofluorescence staining and quantitative analysis of the mean fluorescence intensity for iNOS expression after various treatments. Data are presented as mean ± s.d. (*n* = 3 biologically independent samples). **g** ELISA assay of TNF-α, IL-6, IL-10, and VEGF in RAW 264.7 cells after different treatments in vitro. Data are presented as mean ± s.d. (*n* = 3 biologically independent samples). **h**, **i** The representative images and relative expression quantification of TNF-α were detected by immunohistochemical staining of peripheral tissues after different treatments on the day 5 in vivo, and the positive areas were highlighted by brown staining. Data are presented as mean ± s.d. (*n* = 3 biologically independent samples). **j**, **k** The representative images and relative expression quantification of iNOS were detected by immunohistochemical staining of peripheral tissues after different treatments on the day 5 in vivo, and the positive areas were highlighted by brown staining. Data are presented as mean ± s.d. (*n* = 3 biologically independent samples). **l** ELISA assay of TNF-α, IL-6, IL-10, and VEGF in peripheral tissues after different treatments on the day 5 in vivo. Data are presented as the mean ± s.d. (*n* = 3 biologically independent samples). Statistical significance was assessed using one-way ANOVA with Tukey's multiple comparison test.

in the Motor@CP + NIR group, suggesting successful modulation of the inflammatory process (Fig. 6j and Supplementary Fig. 49). Giemsa staining further confirmed the high efficacy of the Motor@CP + NIR treatment in reducing bacterial infiltration into peripheral tissues. As illustrated in Fig. 6j, while bacterial infiltration was evident in the Control, Motor, CP, and Motor@CP groups, with varying degrees of bacterial clusters and tissue damage, the Motor@CP + NIR group demonstrated a significant reduction in bacterial accumulation. The minimal bacterial infiltration observed in this group underscores the superior efficacy of the Motor@CP + NIR treatment in limiting bacterial vability and promoting a optimal healing environment.

Routine blood tests, including measurements of white blood cells (WBC), red blood cells (RBC), lymphocytes, and neutrophils, revealed significantly elevated WBC, lymphocyte, and neutrophils counts in the Control, CP, Motor, and Motor@CP groups, which could be attributed to residual biofilm infections in the wounds. In contrast, the Motor@CP + NIR group showed a significant decrease in inflammatory cell counts, particularly neutrophils and lymphocytes, reflecting the effective eradication of IABIs in vivo (Supplementary Fig. 50). Furthermore, blood biochemistry analyses revealed that the levels of critical biomarkers remained within normal reference ranges across all treatment groups, indicating no significant hepatic or renal dysfunction (Supplementary Fig. 51). Histological examination via H&E staining of major organs, also showed no lesions or signs of tissue damage in any of the groups (Supplementary Fig. 52). The lack of histopathological abnormalities in these vital organs suggests that the treatments did not result in acute or chronic toxicity, thereby confirming their safety for in vivo applications.

Evaluation of immunomodulatory capability

The impact of Motor@CP on macrophage modulation was further examined. Similarly, a 2.0-mm-thick pork ham slice as a skin substitute was utilized to mimic the clinical scenario (Supplementary Fig. 53). Flow cytometry analysis revealed that Motor@CP + NIR significantly promoted RAW 264.7 macrophages toward a pro-inflammatory M1 phenotype, with an 8.1-fold increase compared to the Control group (Fig. 7a, b and Supplementary Fig. 54). Given that immunosuppressive BME is dominated by the anti-inflammatory M2 phenotype, we further investigated the reprogramming effect from the anti-inflammatory M2 to the pro-inflammatory M1 phenotype. The results demonstrated that Motor@CP + NIR group modulated the shift from CD206 (marker of M2 macrophages) to CD86 (marker of M1 macrophages), effectively reversing the immunosuppressive BME and enhancing the bactericidal immune response (Fig. 7c, d and Supplementary Fig. 55). Immunofluorescence staining was conducted to evaluate the expression of inducible nitric oxide synthase (iNOS), a well-established marker for M1 polarization. The results demonstrated that Motor@CP + NIR-treated macrophages exhibited robust iNOS fluorescence, consistent with the flow cytometry results findings indicating M1 polarization (Fig. 7e, f). Furthermore, the study systematically examined alterations in inflammatory factors using enzyme-linked immunosorbent assays (ELISAs) in vitro. The results revealed that Motor@CP + NIR significantly promoted the secretion of pro-inflammatory cytokines, such as TNF-α and IL-6, thereby providing evidence for the activation of pro-inflammatory macrophage-mediated antibacterial immune responses (Fig. 7g).

On the 5th day of the therapeutic process in murine IABIs models, the infection-draining lymph nodes (IDLNs) were harvested post-sacrifice. Flow cytometry results indicated that Motor@CP + NIR markedly enhanced the pro-inflammatory M1 macrophage polarization (Supplementary Figs. 56a, b, and 57). Furthermore, peripheral tissue from infected areas was collected, and immunohistochemical staining was performed. TNF-α and iNOS were markedly overexpressed in the CP, Motor@CP and Motor@CP + NIR groups, thereby enhancing M1 macrophage migration and restoring their bactericidal potential (Fig. 7h–k). Moreover, ELISA assays of peripheral tissues from infected areas revealed that pro-inflammatory cytokines TNF-α and IL-6 were significantly elevated in the CP, Motor@CP, and Motor@CP + NIR groups, while anti-inflammatory cytokines IL-10 and VEGF were significantly reduced (Fig. 7l). Collectively, these data demonstrate that Motor@CP + NIR effectively promotes the immunomodulation of infiltrating macrophages toward a pro-inflammatory M1 phenotype, thereby enhancing antimicrobial immune responses. Furthermore, at day 10 post-infection, additional ELISA analyses were conducted to validate the immunomodulatory effects on infection control and tissue repair. The results demonstrated that Motor@CP + NIR successfully eradicated biofilm infections, significantly enhanced the expression levels of VEGF and IL-10, and promoted the transition of tissues toward repair in the late stage of anti-IABIs treatment (Supplementary Fig. 58).

Discussion

Copper ions have demonstrated relative stability in the environment, exhibiting resistance to decomposition while maintaining consistent antimicrobial efficacy[34–36]. However, the dense structure of biofilms significantly hinders the uptake of copper ions by bacteria, posing a considerable challenge for current copper-based treatments[23,24]. Our in vitro studies indicate that conventional copper donors, such as $CuCl_2·2H_2O$, result in limited intracellular accumulation of copper ions and exhibit reduced effectiveness against biofilms compared to planktonic bacteria, even at concentrations deemed safe. Notably, bacteria residing within biofilm shelters display heterogeneous physiological activities to adapt to the complicated BME, thereby diminishing therapeutic efficacy and contributing to persistent infections and relapse[7,49]. For instance, bacteria situated deeper within the biofilm demonstrate reduced metabolic activity and lower sensitivity to therapeutic agents due to restricted access to oxygen and nutrients[3,9]. Furthermore, the protective EPS matrix shields bacteria from certain antibiotics, metal cations, and host immune defenses, significantly impeding bacterial clearance and continuously promoting immune evasion[23]. Consequently, overcoming the dense biofilm barrier and extensively delivering copper ions is essential for effective treatment of IABIs.

Untrasmall CP nanoparticles can simultaneously decompose into copper(II) and H_2O_2 in response to an acidic microenvironment. This process further generates •OH via a Fenton-like reaction catalyzed by copper ions. The elevated levels of •OH contributes to disrupting biofilms while enhancing the influx of copper ions. Our in vitro experiments demonstrate that CP treatment partially increases intracellular uptake of copper ions and outperformes $CuCl_2{\cdot}2H_2O$ in terms of biofilm removal efficiency. These findings suggest that CP nanodots can serve as a promising copper ion donor for the treatment of biofilm-associated infections. Nevertheless, within the context of complicated and refractory IABIs, monotherapy with CP remains limited by inadequate penetration into biofilms and insufficient autonomous diffusion within their matrices; thus necessitating the utilization of appropriate nanocarriers.

Nanomotors, characterized by superior autonomous motion capabilities, exhibit considerable potential for overcoming barriers posed by biofilms while facilitating diffusion within these structures and enhancing antibiofilm efficacy[28]. This study proposes a strategy utilizing self-thermophoretic *Janus* bisphere nanomotors loaded with CP for enhanced delivery purposes. Our findings indicate that the rational design of the nanomotor structure, characterized by a mass ratio of 1:1.5 (MSN/Au), achieves an optimal *Janus* bisphere configuration. Leveraging asymmetric NIR laser absorption, our Motor@CP exhibits NIR-propelled self-thermophoretic propulsion and successfully penetrating the biofilm barriers of *S. aureus* and *E. coli*. Even under simulated subcutaneous conditions covered by a 2-mm-thick slice of pork ham, the biofilm penetration ratio of Motor@CP + NIR demonstrates an 14.2-fold higher than that of the single CP group.

As a critical component of the rigid structure of biofilms, eDNA plays a crucial role in the formation, maturation and structural stability of biofilms[43,44]. Our data demonstrate that Motor@CP + NIR can extensively destroy the eDNA component due to its autonomous motion and self-supplying H_2O_2 generation, thereby significantly compromising the integrity and permeability of biofilms and rendering their architecture more amenable to penetration by Motor@CP. Moreover, there is a positive correlation between bacterial viability and biofilm integrity. The penetration of Motor@CP into the biofilm enhances the delivery and decomposition of CP, leading to intracellular accumulation of copper ions that induce cuproptosis-like death in bacteria. This bacterial death compromises the structural support of the biofilm, further facilitating the penetration of Motor@CP. Overall, the ability of nanomotors to penetrate different types of bacterial biofilms is influenced not only by their mechanical motion but also by the degradation of eDNA components within biofilms via •OH. Additionally, the process of biofilm penetration is enhanced by the reduction in bacterial viability attributed to cuproptosis-like death. Collectively, these effects demonstrate the synergistic action of multiple mechanisms across various bacterial biofilm types, providing valuable insights for future medical applications from our Motor@CP.

Additionally, reversing the biofilm-induced immunosuppressive microenvironment remains a critical challenge for biofilm eradication[12,15]. In IABIs, the biofilm microenvironment polarizes immune cells toward an anti-inflammatory phenotype, characterized by a shift to the macrophage M2 phenotype and impaired phagocytosis, thereby hindering bacterial killing[5,8]. An ideal approach for eradicating IABIs should aim at eliminating bacterial biofilms while repolarizing M2 macrophages to an antimicrobial M1 phenotype; thereby further targeting exposed planktonic bacteria and preventing re-colonization. In this study, our Motor@CP, at the same concentrations as the antibiofilm dose, induces M0 macrophages to polarize into the M1 phenotype and reprograms M2 macrophages to the M1 phenotype under the above-simulated subcutaneous conditions. This process restores their impaired immune function and effectively clears biofilm infections by promoting the release of pro-inflammatory cytokines (e.g., TNF-α, IL-6). Overall, this integrated therapeutic approach, which combines intrinsic biofilm removal with immune modulation, successfully eradicates persistent IABIs, offering a promising avenue for improving current therapeutic strategies and holding significant potential for further medical applications.

Methods

This research complies with all applicable ethical regulations. The animal experiments were approved by the Institutional Committee on the Ethics of Animal Experiments at Zhengzhou University (Approval No. 2023-KY-0433-001, Zhengzhou, China). All animal procedures were conducted in accordance with the Guide for the Care and Use of Laboratory Animals published by the National Institutes of Health.

Preparation of CP (CuO_2-PVP) nanodots

CP nanodots were synthesized following a previously established protocol[22]. Briefly, $CuCl_2{\cdot}2H_2O$ (0.01 M) was dissolved in 5 ml of double-distilled water (ddH_2O). Then, 5 ml of NaOH (0.02 M) and 0.5 g of PVP (Mw 10,000) were sequentially added, and the solution was ultrasonicated until it became transparent. Finally, 100 µl of H_2O_2 was added and stirred for 30 min to form the CP nanodots. The reaction product was further transferred to a 50 ml centrifuge tube equipped with a 30 kDa molecular weight cutoff filter membrane (Sigma), centrifuged at 3358 × *g* for 25 min, and subsequently washed with ddH_2O. The entire process was performed three times.

Preparation of mesoporous silica nanoparticles (MSNs) and gold nanoparticles (AuNPs)

MSNs were synthesized using a one-pot method with CTAB and NaSal as structure-directing agents, TEOS as the silicon precursor, and TEA as the catalyst[50]. The process involved dissolving 68 mg of TEA in 25 ml of water and heating it at 80 °C for 30 min, followed by the addition of 380 mg of CTAB and 80 mg of NaSal. After stirring for 1 h, 4 ml of TEOS was added, and the reaction continued for 2 h. The product was collected by centrifugation, washed with ethanol, and extracted with HCl-methanol at 60 °C for 6 h, repeated three times to remove the template. Finally, the product was vacuum-dried overnight. AuNPs were synthesized using a modified citrate reduction method. Specifically, 50 ml of 0.25 mM $HAuCl_4$ solution was heated to boiling in a 100 ml round-bottom flask. Under vigorous stirring, 1.5 ml of 1% sodium citrate solution was rapidly added. The mixture was refluxed for 10 min and stirred for an additional 15 min after heating to obtain the gold seed solution. Subsequently, 1 ml of 1% $HAuCl_4$, 4 ml of 1% sodium citrate, and 1 ml of the gold seed solution were mixed and diluted to 10 ml with ultrapure water. Next, 0.1 ml of 30% H_2O_2 was added under magnetic stirring for 5 min. Finally, the mixture was centrifuged to remove unreacted reagents, and the precipitate was resuspended in ultrapure water.

Preparation of MSN-Au *Janus* bisphere nanomotors (Motors)

The MSN-Au *Janus* bisphere nanomotors were synthesized using the Pickering emulsion method[40]. 0.8 g of paraffin wax and MSN (20 mg) were dispersed in an aqueous solution (10 ml, 6.7% ethanol), and CTAB was added (208 µl, 1 µM). The solution was heated to 80 °C until the paraffin was completely melted and stirred for 1 h at 75 °C using an Ultra-Turrax T-8 (IKA, Germany) at 1776 × *g* to form a stable emulsion. After cooling, the mixture was diluted with methanol (10 ml), and (3-mercaptopropyl)trimethoxysilane (200 µl) was added, followed by 3 h of magnetic stirring. The solid was isolated by centrifugation, washed, and the partially thiol-functionalized MSNs were mixed with AuNPs in Tris-HCl buffer (pH 8.5). After overnight stirring, the solid was filtered, washed with chloroform, and dried to yield the nanomotors.

Preparation of Motor@CP

CP (4 mg) was first dissolved in 5 ml of ddH_2O, and then 20 mg of Motor was added to the solution. The mixture was stirred overnight and subsequently centrifuged at 15978 × *g* for 5 min. The resulting precipitate was collected, yielding the CP-loaded Motor (Motor@CP) as the final product.

In vitro biofilm penetration

Firstly, the density of *S. aureus* and *E. coli* was diluted to 10^6 CFU ml^{-1} to cultivate biofilm in the confocal microscopy plate (Biosharp, China). After 3 days of cultivation at 37 °C, mature biofilms were developed in the confocal dishes. To evaluate the penetration capacity of nanoparticles, the biofilms were stained by SYTO 9 (6 μM, 50 μl) for 30 min in the dark, and the Motor was labeled with rhodamine B. In addition, the CP group alone was also labeled with rhodamine B. After receiving treatments with CP, Motor@CP, Motor + NIR, and Motor@CP + NIR (808 nm, 5 min, 1.0 W cm^{-2}), the sample was gently washed three times with sterile PBS to remove nanoparticles adhering to the outer surface of the biofilm. The relevant images were captured and analyzed by CLSM (Leica SP-8, Germany).

In vitro antibiofilm effcacy

Bacterial suspensions of *S. aureus*, MRSA, and *E. coli* (10^6 CFU ml^{-1}) were inoculated into 24-well plates and incubated for 3 days to form biofilms. Treatments included: Control, CP, Motor, Motor@CP, and Motor@CP + NIR (808 nm, 5 min, 1.0 W cm^{-2}). After treatment, biofilms were stained with crystal violet and measured at 590 nm using an enzyme reader (Bio-TEK, Synergy H1, USA). For SPM, biofilms were disrupted, serially diluted, and plated on Columbia blood agar plates (CNA) to count bacterial colonies after overnight incubation. To examine biofilm disruption, biofilms were stained with SYTO 9 and PI, and their structure was observed using CLSM (Leica SP-8, Germany). Finally, *S. aureus*, MRSA, and *E. coli* biofilms were fixed with 2.5% glutaraldehyde at 4 °C for 12 h, then dehydrated using ethanol gradients (30–100%), with each gradient lasting 10 min. After dehydration, the samples were placed in a critical point dryer for approximately 1 h. Finally, the samples were fixed onto the specimen holder using conductive adhesive tape, gold-coated, and prepared for testing using SEM (Hitachi SU8010, Japan).

Evaluation of therapeutic effect in vivo

To establish the murine IABIs models, male Balb/C mice (8 weeks, 20–25 g) were purchased from Beijing Weitong Lihua Experimental Animals and all mice were maintained in a specific pathogen-free environment. The animal experiments were approved by the Institutional Committee on the Ethics of Animal Experiments at Zhengzhou University (Approval No. 2023-KY-0433-001, Zhengzhou, China). All animal procedures were conducted in accordance with the Guide for the Care and Use of Laboratory Animals published by the National Institutes of Health. The findings of this study exhibit broad applicability across different genders. The mice were anesthetized with isoflurane and underwent surgery to implant PEEK washers pre-formed with biofilms on the back of the neck. After suturing, the mice were divided into five treatment groups: Control, CP, Motor, Motor@CP, and Motor@CP + NIR (808 nm, 1.0 W cm^{-2}, 5 min). The CP concentration was set at 4 mg kg^{-1} for the CP and Motor@CP groups. Over a 10-day period, changes in the infected area and body weight were monitored. At the end of the study, mice were euthanized, and samples were collected for microbiological analysis, SEM imaging, and histological evaluation.

Evaluation of immune response in vitro and in vivo

RAW 264.7 cells (3.0×10^6 cells ml^{-1}) were cultured in 6-well plates and treated with CP, Motor, Motor@CP, and Motor@CP + NIR (4 μg ml^{-1}, in terms of CP) in DMEM-H containing 2 mM GSH for 24 h. Prior to NIR irradiation, a 2-mm-thick slice of pork ham was positioned directly above the perforated plate. After the treatment period, the cells were harvested by scraping and then centrifuged to isolate the cell pellets. To assess the macrophage activation, flow cytometry (BD FACSCanto II, USA) was performed. The expression levels of CD86 (a marker for M1 macrophage activation) and F4/80 (a macrophage marker) were measured using APC-labeled and FITC-labeled antibodies, respectively. This allowed for quantification of the macrophage phenotype after treatments.

For the evaluation of the immunosuppressive reprogramming model in the biofilm infection microenvironment, RAW 264.7 cells (3.0×10^6 cells ml^{-1}) were induced with IL-4 and IL-13 for 24 h to polarize them toward the anti-inflammatory M2 phenotype and subsequently treated with different conditions in DMEM-H containing 2 mM GSH for an additional 24 h[51]. Prior to NIR irradiation, a 2-mm-thick pork ham slice was placed directly above the wells of the microplate. To assess macrophage polarization, flow cytometry (BD FACSCanto II, USA) was performed. The expression levels of CD86 and CD206 (markers of M2 macrophage activation) were measured using PE-labeled and FITC-labeled antibodies, respectively.

For immunofluorescent staining, RAW 264.7 cells (3.0×10^6 cells ml^{-1}) treated with CP, Motor, Motor@CP, and Motor@CP + NIR (4 μg ml^{-1}, in terms of CP) were fixed with 4% paraformaldehyde for 10 min, blocked with Immunostaining Blocking Solution (Beyotime, China) for 30 min, and incubated overnight at 4 °C with anti-iNOS antibody (Abcam, USA). After washing, cells were incubated with the CoraLite® Plus 488-Goat Anti-Rabbit secondary antibody (Proteintech, China) for 1 h at room temperature, followed by DAPI (Servicebio, China) staining for nuclei. Finally, the samples were visualized using a confocal microscope (ZEISS LSM 710, Germany).

Mice were sacrificed 5 days post-infection for in vivo immune evaluation of IABIs. Infected-draining lymph nodes (IDLNs) from both axillae were collected, chopped, and digested with an enzyme mixture at 37 °C for 30 min. The resulting cell suspensions were filtered through a 70 μm mesh to obtain single-cell suspensions. These were stained with Fixable Viability Stain 780 to exclude dead cells, then labeled with flow cytometry antibodies (anti-CD45-FITC, anti-CD11b-PerCp-Cy5.5, anti-F4/80-PE, anti-CD86-PE-Cy7, anti-CD206-APC) and analyzed using a flow cytometer (BD FACSMelody, USA). Detailed information regarding all the antibodies used in this study is provided in the Supplementary Table 2.

Statistical analysis

The data are expressed as the mean ± s.d. The data were analyzed using GraphPad Prism software (GraphPad Prism 8). All statistical analyses are stated specifically in the figure legends for all experiments. For most experiments, unless otherwise specified in the figure legend, one-way analysis of variance (ANOVA) was performed with Tukey's multiple comparisons test. Two-way ANOVA with Tukey's multiple comparisons test was used in Fig. 2 and Fig. 5c. An unpaired two-tailed Student's *t*-test was used in Fig. 4b. Statistical significance was shown in figure. NS, not significant.

Reporting summary

Further information on research design is available in the Nature Portfolio Reporting Summary linked to this article.

Data availability

The authors declare that all data supporting the findings of this study are available within the article, the Supplementary Information and Source Data file. The RNA-seq data generated in this study have been deposited in the BioProject database under accession code SRX26959086. All data are available from the corresponding author upon request.

References

1. Patel, R. Periprosthetic joint infection. *N. Engl. J. Med.* **388**, 251–262 (2023).

2. Arciola, C. R., Campoccia, D. & Montanaro, L. Implant infections: adhesion, biofilm formation and immune evasion. *Nat. Rev. Microbiol.* **16**, 397–409 (2018).
3. Flemming, H.-C. et al. Biofilms: an emergent form of bacterial life. *Nat. Rev. Microbiol.* **14**, 563–575 (2016).
4. Stewart, P. S. & Bjarnsholt, T. Risk factors for chronic biofilm-related infection associated with implanted medical devices. *Clin. Microbiol. Infect.* **26**, 1034–1038 (2020).
5. Wu, Y. K., Cheng, N. C. & Cheng, C. M. Biofilms in chronic wounds: pathogenesis and diagnosis. *Trends Biotechnol.* **37**, 505–517 (2019).
6. Guo, H. et al. Biofilm and small colony variants—an update on staphylococcus aureus strategies toward drug resistance. *Int. J. Mol. Sci.* **23**, 1241 (2022).
7. Ciofu, O., Moser, C., Jensen, P. & Ø.&Høiby, N. Tolerance and resistance of microbial biofilms. *Nat. Rev. Microbiol.* **20**, 621–635 (2022).
8. Guo, G. et al. Space-selective chemodynamic therapy of $CuFe_5O_8$ nanocubes for implant-related infections. *ACS Nano* **14**, 13391–13405 (2020).
9. Choi, V., Rohn, J. L., Stoodley, P., Carugo, D. & Stride, E. Drug delivery strategies for antibiofilm therapy. *Nat. Rev. Microbiol.* **21**, 555–572 (2023).
10. Rumbaugh, K. P. & Sauer, K. Biofilm dispersion. *Nat. Rev. Microbiol.* **18**, 571–586 (2020).
11. Zhu, W. et al. Photothermal nanozyme-based microneedle patch against refractory bacterial biofilm infection via iron-actuated janus ion therapy. *Adv. Mater.* **34**, e2207961 (2022).
12. Xu, D. et al. Nanoadjuvant-triggered STING activation evokes systemic immunotherapy for repetitive implant-related infections. *Bioact. Mater.* **19**, 102–116 (2024).
13. Kim, B.-E., Nevitt, T. & Thiele, D. J. Mechanisms for copper acquisition, distribution and regulation. *Nat. Chem. Biol.* **4**, 176–185 (2008).
14. Tsvetkov, P. et al. Copper induces cell death by targeting lipoylated TCA cycle proteins. *Science* **375**, 1254–1261 (2022).
15. Li, S. et al. Ultrasound-activated probiotics vesicles coating for titanium implant infections through bacterial cuproptosis-like death and immunoregulation. *Adv. Mater.* **36**, e2405953 (2024).
16. Xu, Y. et al. An enzyme-engineered nonporous copper(I) coordination polymer nanoplatform for cuproptosis-based synergistic cancer therapy. *Adv. Mater.* **34**, e2204733 (2022).
17. Xue, Y. et al. Low-dose Cu ions assisted by mild thermal stimulus inducing bacterial cuproptosis-like death for antibiosis and biointegration. *Adv. Funct. Mater.* **34**, 2308197 (2023).
18. Huang, Y. et al. Ultrasound-activated piezo-hot carriers trigger tandem catalysis coordinating cuproptosis-like bacterial death against implant infections. *Nat. Commun.* **15**, 1643 (2024).
19. Mei, J. et al. Biofilm microenvironment-responsive self-assembly nanoreactors for all-stage biofilm associated infection through bacterial cuproptosis-like death and macrophage re-rousing. *Adv. Mater.* **35**, e2303432 (2023).
20. Xu, D. et al. Self-homeostasis immunoregulatory strategy for implant-related infections through remodeling redox balance. *ACS Nano* **17**, 4574–4590 (2023).
21. Xiao, J. et al. Self-enhanced ROS generation by responsive co-delivery of H_2O_2 and O_2 based on a versatile composite biomaterial for hypoxia-irrelevant multimodal antibiofilm therapy. *Chem. Eng. J.* **465**, 142958 (2023).
22. Lin, L. S. et al. Synthesis of copper peroxide nanodots for H_2O_2 self-supplying chemodynamic therapy. *J. Am. Chem. Soc.* **141**, 9937–9945 (2019).
23. Flemming, H. C. & Wingender, J. The biofilm matrix. *Nat. Rev. Microbiol.* **8**, 623–33 (2010).
24. Lv, X. et al. Recent nanotechnologies to overcome the bacterial biofilm matrix barriers. *Small* **19**, e2206220 (2023).
25. Ladomersky, E. & Petris, M. J. Copper tolerance and virulence in bacteria. *Metallomics* **7**, 957–964 (2015).
26. Cooksey, D. A. Copper uptake and resistance in bacteria. *Mol. Microbiol.* **7**, 1–5 (1993).
27. Wu, Z. et al. Oral mitochondrial transplantation using nanomotors to treat ischaemic heart disease. *Nat. Nanotechnol.* **19**, 1375–1385 (2024).
28. Sun, B., Kjelleberg, S., Sung, J. J. Y. & Zhang, L. Micro- and nanorobots for biofilm eradication. *Nat. Rev. Bioeng.* **2**, 367–369 (2024).
29. Wang, Z. H. et al. Biological chemotaxis-guided self-thermophoretic nanoplatform augments colorectal cancer therapy through autonomous mucus penetration. *Sci. Adv.* **8**, eabn3917 (2022).
30. Wang, Z.-H. et al. Bioactive nanomotor enabling efficient intestinal barrier penetration for colorectal cancer therapy. *Nat. Commun.* **16**, 1678 (2025).
31. Zhang, X., Fu, Q., Duan, H., Song, J. & Yang, H. Janus nanoparticles: from fabrication to (bio) applications. *ACS Nano* **15**, 6147–6191 (2021).
32. Liu, Z. et al. Janus nanoparticles targeting extracellular polymeric substance achieve flexible elimination of drug-resistant biofilms. *Nat. Commun.* **14**, 5132 (2023).
33. Ji, X. et al. Multifunctional parachute-like nanomotors for enhanced skin penetration and synergistic antifungal therapy. *ACS Nano* **15**, 14218–14228 (2021).
34. Liu, F. et al. Synergistic wall digestion and cuproptosis against fungal infections using lywallzyme-induced self-assembly of metal-phenolic nanoflowers. *Nat. Commun.* **15**, 9004 (2024).
35. Frei, A., Verderosa, A. D., Elliott, A. G., Zuegg, J. & Blaskovich, M. A. T. Metals to combat antimicrobial resistance. *Nat. Rev. Chem.* **7**, 202–224 (2023).
36. Zhang, E. et al. Antibacterial metals and alloys for potential biomedical implants. *Bioact. Mater.* **6**, 2569–2612 (2021).
37. Ning, C. et al. Concentration ranges of antibacterial cations for showing the highest antibacterial efficacy but the least cytotoxicity against mammalian cells: implications for a new antibacterial mechanism. *Chem. Res. Toxicol.* **28**, 1815–1822 (2015).
38. Karygianni, L., Ren, Z., Koo, H. & Thurnheer, T. Biofilm matrixome: extracellular components in structured microbial communities. *Trends Microbiol.* **28**, 668–681 (2020).
39. Jia, C., Guo, Y. & Wu, F.-G. Chemodynamic therapy via Fenton and Fenton-like nanomaterials: strategies and recent advances. *Small* **18**, 2103868 (2021).
40. Díez, P. et al. Ultrafast directional Janus Pt–mesoporous silica nanomotors for smart drug delivery. *ACS Nano* **15**, 4467–4480 (2021).
41. Liu, C. et al. Near-infrared AIE dots with chemiluminescence for deep-tissue imaging. *Adv. Mater.* **32**, 2004685 (2020).
42. Miao, Q. & Pu, K. Organic semiconducting agents for deep-tissue molecular imaging: second near-infrared fluorescence, self-luminescence, and photoacoustics. *Adv. Mater.* **30**, 1801778 (2018).
43. Whitchurch, C. B., Tolker-Nielsen, T., Ragas, P. C. & Mattick, J. S. Extracellular DNA required for bacterial biofilm formation. *Science* **295**, 1487 (2002).
44. Fulaz, S., Vitale, S., Quinn, L. & Casey, E. Nanoparticle-biofilm interactions: the role of the EPS matrix. *Trends Microbiol.* **27**, 915–926 (2019).
45. Solmonson & A.&DeBerardinis, R. J. Lipoic acid metabolism and mitochondrial redox regulation. *J. Biol. Chem.* **293**, 7522–7530 (2017).
46. Rowland, E. A., Snowden, C. K. & Cristea, I. M. Protein lipoylation: an evolutionarily conserved metabolic regulator of health and disease. *Curr. Opin. Chem. Biol.* **42**, 76–85 (2017).

47. Cronan, J. E. Assembly of lipoic acid on its cognate enzymes: an extraordinary and essential biosynthetic pathway. *Microbiol. Mol. Biol. Rev.* **80**, 429–450 (2016).
48. Su, Z. et al. Bioresponsive nano-antibacterials for H_2S-sensitized hyperthermia and immunomodulation against refractory implant–related infections. *Sci. Adv.* **8**, eabn1701 (2022).
49. Harrison, J. J., Ceri, H. & Turner, R. J. Multimetal resistance and tolerance in microbial biofilms. *Nat. Rev. Microbiol.* **5**, 928–938 (2007).
50. Yang, Y. et al. Anion assisted synthesis of large pore hollow dendritic mesoporous organosilica nanoparticles: understanding the composition gradient. *Chem. Mater.* **28**, 704–707 (2016).
51. Zhang, M.-Z. et al. IL-4/IL-13-mediated polarization of renal macrophages/dendritic cells to an M2a phenotype is essential for recovery from acute kidney injury. *Kidney Int.* **100**, 1034–1043 (2016).

Acknowledgements

This work was financially supported by the National Natural Science Foundation of China (Grant No. 82102588, 82102936), the Clinical Medical Scientist of Henan Academy of Innovations in Medical Science (Grant No. HNCMS20240059), the Young Elite Scientists Sponsorship Program by CAST (Grant No. 2023QNRC001), the Natural Science Foundation of Henan Province (Grant No. 232300421050, 242301420068), the China Postdoctoral Science Foundation (Grant No. 2023M743232), the Postdoctoral Fellowship Program of CPSF (Grant No. GZB20230676), the Young and Middle-Aged Discipline Leader of Henan Provincial Health Commission (Grant No. HNSWJW2022007), and the Medical Science and Technology Research Project of Henan Province (Grant No. LHGJ20230207). The manuscript of Fig. 3m were created with BioRender.com.

Author contributions

D.L., J.S., Z.W. (Zhi-Hao Wang), and C.Z. conceived and designed the study. L.H., Q.P., and M.L. performed the in vivo experiments. L.H., Z.W. (Zhichao Wang), and L.W. performed the in vitro experiments. L.H. and Q.P. contributed to the analysis and interpretation of the results. D.L., J.S., and Z.W. (Zhi-Hao Wang) contributed to writing of the manuscript.

Competing interests

The authors declare no competing interests.

Additional information

Supplementary information The online version contains supplementary material available at https://doi.org/10.1038/s41467-025-64064-z.

Correspondence and requests for materials should be addressed to Chi Zhang, Zhi-Hao Wang, Jinjin Shi or Daifeng Li.

Peer review information *Nature Communications* thanks Zheng Su, XianZeng Zhang, and the other, anonymous, reviewer for their contribution to the peer review of this work. A peer review file is available.